A. BOGAERTS[1],✉
M. GROZEVA[2]

Axial non-uniformity of longitudinal hollow-cathode discharges for laser applications: numerical modeling and comparison with experiments

[1] University of Antwerp, Department of Chemistry, Universiteitsplein 1, 2610 Wilrijk–Antwerp, Belgium
[2] Institute of Solid State Physics, Bulgarian Academy of Sciences, 72 Tzarigradsko Chaussee, 1784 Sofia, Bulgaria

ABSTRACT It is demonstrated by means of numerical modeling that longitudinal hollow-cathode discharges (HCDs) typically used for laser applications are strongly non-uniform in the axial direction. Two kinds of HCDs are investigated; those having one anode ring and those having two anode rings at opposite ends of the HCD tube. The HCD under study was made of copper and operated in a mixture of helium and argon. The calculated potential varied considerably in the axial direction. The densities of the major plasma species showed no maxima in the middle of the HCD, but rather at the anode side(s). The same applied to the sputtering rate at the cathode and the electron-impact ionization and excitation rates in the plasma. The calculation results for both configurations have been compared with measured data, i.e. with the electric current and the optical emission intensities of He (I) and Cu (I) lines as a function of axial position, and reasonable agreement has been reached.

PACS 52.65.-y; 52.65.Ww; 42.55.L

1 Introduction

Hollow-cathode discharges (HCDs) are used in laser technology [1, 2], in atomic spectrometry [3, 4] and for processing applications, such as etching, deposition and surface modification [5]. Depending on the position of the hollow-cathode cylinder and the anode with respect to each other, two basic types of discharges can be distinguished in cylindrical HCDs [6–10]:

(i) Transverse discharges. The electrode configuration creates an electric field and a discharge current transverse to the hollow-cathode axis (e.g. anode placed inside the HCD tube).

(ii) Longitudinal discharges. As a result of the positioning of the anode outside the HCD tube, the electrons leaving the cathode surface move towards the anode along the hollow-cathode axis, due to the axial (longitudinal) electric field.

Whereas transverse discharges are generally uniform in the axial direction, this is not the case for longitudinal discharges. Indeed, due to the longitudinal flow of electrons, the latter kind of HCDs can be severely non-uniform in the axial

direction. Mizeraczyk [7, 8] has experimentally investigated the axial non-uniformity of longitudinal HCDs. Characteristic plasma quantities, such as the plasma potential [7, 8], the current density at the cathode [7], the electron energy distribution function and the mean electron energy and electron density [8] have been measured as a function of axial position in HCD tubes with varying lengths, and for a wide range of pressures and electric currents. It has been demonstrated that the axial non-uniformity increases with decreasing pressure and current, and is more pronounced in long discharge tubes with small diameters, typically used for laser applications [7, 8].

Mizeraczyk has also compared the laser properties of transverse and longitudinal HCDs [9, 10]. Whereas the He-Kr$^+$ laser showed some advantages with the transverse HCD for lasing at 469.4 nm [9], the important white-light He-Cd$^+$ laser, which results from simultaneous lasing at the three basic lines (blue, green and red) was found to be superior in the longitudinal HCD [10].

Because the axial non-uniformity of the longitudinal HCD may affect the operation of the laser [7], a good knowledge of the axial variation of characteristic plasma quantities is desirable. Beside experimental investigations [7, 8], this can also be obtained by numerical modeling. In the present paper, we want to investigate the axial non-uniformity of longitudinal HCDs by means of a hybrid modeling network, which was recently developed for a copper HCD in a mixture of helium with argon, typically used as a He-Cu$^+$ IR laser [11]. Moreover, the calculation results will be compared with experimental data for exactly the same conditions and HCD tube design.

In Sect. 2, a short description of the modeling network will be given. The experimental set-up will be described in Sect. 3. The calculation results, as well as the comparison with the experimental data, will be presented in Sect. 4. Finally, a conclusion will be given in Sect. 5.

2 Description of the model

The plasma species assumed to be present in the helium–argon–copper HCD are the He and Ar gas atoms, the electrons, the He$^+$, He$_2^+$, Ar$^+$ and Ar$_2^+$ ions, the metastable He and Ar atoms (He$_m^*$ and Ar$_m^*$), fast He and Ar atoms, the sputtered Cu atoms and the corresponding Cu$^+$ ions. No specific model is applied to the He and Ar gas atoms, which are

✉ Fax: +32/3/820-23-76, E-mail: annemie.bogaerts@ua.ac.be

simply assumed to have thermal velocities and be uniformly distributed in the discharge tube. The other species are described with Monte Carlo and/or fluid models.

The electrons are split into two groups, depending on their energy. Electrons with a total energy (i.e. the sum of their potential and kinetic energies) above the threshold for inelastic collisions with the He, Ar or Cu atoms are called "fast" and are simulated with a Monte Carlo model. Their trajectories during successive time steps are calculated with Newton's laws, and the collisions during these time steps (i.e. the occurrence of a collision, the kind of collision, and new energy and direction after collision) are treated with random numbers. The collision processes taken into account include elastic collisions with He and Ar gas atoms, ionization and excitation of He and Ar ground-state atoms and metastable atoms, and ionization of the sputtered Cu atoms.

When the total (kinetic+potential) energy of the electrons drops below the threshold for inelastic collisions, the electrons are transferred to the slow-electron group. Since these electrons cannot give rise to inelastic collisions any more, their only role in the plasma is to provide negative space charge and to carry electric current. Hence, their behavior can as well (and much faster) be described by a fluid code. Besides the slow electrons, this fluid model also treats the He^+, He_2^+, Ar^+ and Ar_2^+ ions. It consists of five continuity equations (i.e. for the five different species) with different production and loss terms, and five transport equations, based on diffusion and on migration in the electric field. Moreover, these ten equations are coupled to Poisson's equation for a self-consistent calculation of the electric field distribution. The production and loss processes incorporated for the electrons and ions are electron-impact ionization (from the He and Ar ground states and metastable levels), different electron–ion recombination mechanisms, ionization and associative ionization (i.e. formation of molecular ions) by collisions of two metastable atoms or by collisions of higher excited atoms with ground-state atoms, Penning ionization by metastable atoms, asymmetric charge transfer of He^+ and Ar^+ ions with Cu atoms and conversion from atomic ions to molecular ions. The processes are described in more detail in [11].

A similar fluid model is also developed for the He_m^* and Ar_m^* metastable atoms. It is again based on continuity equations with different production and loss terms, and transport equations (describing only diffusion). He and Ar both have two metastable levels lying close to each other. However, since we are only interested in the total metastable density, we have combined the two metastable levels in one collective level for He and one for Ar. The production processes taken into account for the metastable levels are electron-impact excitation from the ground state and electron–ion recombination. The loss processes are electron-impact ionization, excitation and de-excitation from the metastable level, Penning ionization, collisions between two metastable atoms, leading to ionization of one of the atoms or to associative ionization, as well as two-body and three-body collisions with ground-state atoms. More information of these mechanisms can again be found in [11].

Besides the ion–electron fluid model, the He^+ and Ar^+ ions are also followed with a Monte Carlo method, which yields complementary information to the fluid code, such as the ion-energy distributions, which are necessary to calculate the flux of sputtered atoms at the cathode. Such a Monte Carlo algorithm is not only applied for the He^+ and Ar^+ ions, but also for the fast He and Ar atoms, which are created by elastic collisions of the He^+ and Ar^+ ions with He and Ar gas atoms. Indeed, due to the large fluxes of fast He and Ar atoms bombarding the cathode, the latter species play a non-negligible role in sputtering [11].

The flux of sputtered Cu atoms at the cathode is calculated based on the flux energy distributions of He^+ and Ar^+ ions and fast He and Ar atoms, as well as Cu^+ ions (see below) bombarding the cathode, which are calculated in Monte Carlo models, multiplied with the corresponding sputtering yields as a function of bombarding energy. The energy of the sputtered Cu atoms is typically in the order of 5–10 eV. They lose this energy, however, rapidly by collisions with the He and Ar gas atoms, until they are thermalized. This thermalization process is described with a Monte Carlo code, and it results in a so-called thermalization profile, i.e. the number of thermalized atoms as a function of distance from the cathode.

The thermalization profile is used as an input in the fluid model for the thermalized Cu atoms and corresponding Cu^+ ions. This fluid model consists again of two continuity equations and two transport equations (based on diffusion of the atoms, and on diffusion and migration of the ions). The production of Cu atoms is given by the sputtering flux multiplied by the thermalization profile. The loss of Cu atoms is equal to the production of Cu^+ ions, and is determined by various ionization mechanisms, i.e. electron-impact ionization, Penning ionization by He_m^* and Ar_m^* atoms and asymmetric charge transfer of Cu atoms with He^+ and Ar^+ ions. No specific loss mechanism is taken into account for the Cu^+ ions, except from recombination at the cell walls (which is determined by the boundary conditions).

Finally, the Cu^+ ions are also subsequently treated with a Monte Carlo algorithm, which allows the calculation of the flux energy distribution of the Cu^+ ions bombarding the cathode, needed to calculate the sputtering flux. The Cu^+ ions indeed play a quite important role in the sputtering process (so-called "self-sputtering") [11].

All these models are coupled to each other into a "modeling network" due to the interaction processes between the different species. Hence, they are solved iteratively until final convergence is reached. The whole calculation procedure typically takes a few days on today's fast computers. Detailed information about this modeling network (i.e. an overview of all collision processes taken into account, and the corresponding cross sections or rate coefficients, as well as details about the coupling of the models) can be found in [11].

3   Experimental set-up

As mentioned above, the results of the modeling network will be compared with experimental data, obtained for the same discharge tube and operating conditions to which the models are applied.

Two kinds of experiments are performed, i.e. (i) measurements of the axial distribution of the current density at the cathode, and (ii) measurements of the optical emission in-

tensities of a He (I) and a Cu (I) line as a function of axial position. Different tube designs were used for these two experiments. They had, however, the same length (5 cm) and inner diameter (4 mm), and were both made of copper, so that both sets of experimental data could be directly compared with the results of the model, which was also applied to a copper HCD with 5-cm length and 4-mm inner diameter.

For the measurement of the current density at the cathode, a segmented tube was used, which consisted of 19 annular segments of 3-mm-thick copper, with inner and outer diameters of 4 mm and 15 mm, respectively (see Fig. 1a). The segments were isolated from each other by 0.3-mm-thick quartz rings. They were mounted in a quartz tube with 15-mm inner diameter. Hence, the discharge could only burn inside the copper rings. Each electrode was connected independently to the electric power supply. By changing the polarity of the segments, different anode–cathode combinations could be made. For the present experiment, two configurations were investigated: (i) an asymmetric discharge, with an anode ring at one side of the HCD (so-called "AC"; anode–cathode); and (ii) a symmetric discharge, with two anode rings at both sides of the HCD ("ACA"; anode–cathode–anode). The current through each segment was measured by recording the voltage drop across a calibrated 4.2-Ω resistor, connected to each segment. A similar segmented tube design, but with somewhat different dimensions and materials, was also used by Mizeraczyk [7].

For the measurement of the light intensity in the axial direction, a slotted-tube design was used (see Fig. 1b). The HCD had a length of 5 cm, and inner and outer diameters of 4 and 8 mm, respectively. Along the length of the tube, a 0.8-mm-wide slit was cut. Two copper ring anodes were placed at both ends of the cathode, of which one could be disconnected. Hence, both the asymmetric (AC) and the symmetric (ACA) tube designs (see above) could be realized. The outer surfaces of the cathode and the anodes were covered with quartz insulation, so that the discharge was again confined in the cathode cavity. The electrodes were mounted in a quartz tube having a side quartz window opposite to the cathode slit, through which the sidelight emission could be monitored.
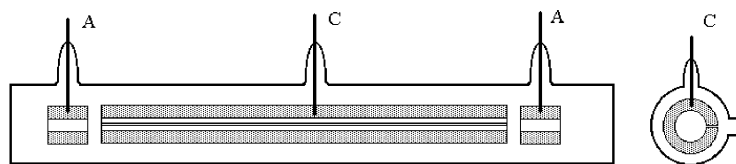
The measuring set-up for the emitted light is shown in Fig. 1c. The light emitted through the cathode slit passed through a 1-mm diaphragm (D), and was focused by a lens (L) at the front end of the optical fiber (OF). The other end of the fiber was mounted at the entrance slit of the Bentham grating monochromator (M). The signal on the photomultiplier (F) of the selected line was monitored by a 200-MHz Tektronix TDS420A oscilloscope (Tek) and stored in a computer (PC). The diaphragm, the lens and the front-end of the optical fiber were mounted on a table, which could be translated along the discharge tube (DT) length, parallel to the cathode slit, with a step of 1 mm. The sidelight emission intensity distribution along the cathode length was measured for two different lines, i.e. a He (I) line at 587.6 nm and a Cu (I) line at 510.6 nm.

a Segmented tube design
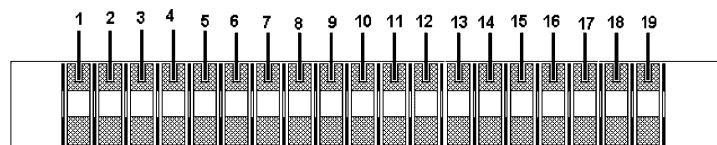
copper segments: 3 mm thick, 4 mm inner and 15 mm outer diameter
quartz rings between segments: 0.3 mm thick
quartz tube: 15 mm inner diameter

b Slotted tube design

copper tube: 5 cm long, 4 mm inner and 8 mm outer diameter
slit along length of tube: 0.8 mm wide

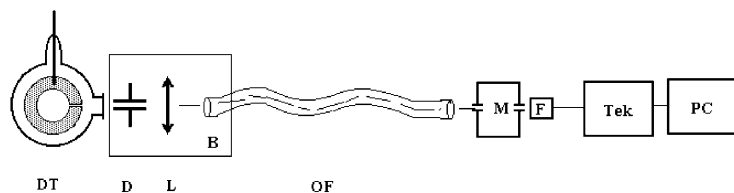**c** Measuring set-up for emitted light

FIGURE 1   Schematic diagrams of the measuring set-up: **a** segmented HCD tube for the current density measurements; **b** slotted HCD tube for the measurement of the optical emission intensities; **c** measuring set-up for the sidelight emission intensity (DT, discharge tube; D, diaphragm; L, lens; OF, optical fiber; M, monochromator; F, photomultiplier; Tek, Tektronix oscilloscope; and PC, computer)

4   Results and discussion

Both the model and experiments were applied to a copper HCD of 5-cm length and 4-mm inner diameter, in a mixture of He with 5% Ar. The total gas pressure was fixed at 17 Torr (2267 Pa), and the electric current was varied between 1 and 3 A. The gas temperature was not measured in the experiment. It was, however, needed as an input in the model, because it determined, in combination with the pressure, the gas density through the ideal gas law ($n = p/kT$). In principle, it is possible to calculate the gas temperature [12], but this would have further complicated our model and increased the computation time. In reality, the gas temperature will exhibit a spatial variation, and it will increase with rising electric current. However, since the actual variation of gas temperature with electric current was not known, we simply assumed a constant value of 1000 K in our model.

As mentioned in Sect. 3, two different electrode configurations were investigated, i.e. the asymmetric HCD (AC) and the symmetric HCD (ACA). In both cases, the anode ring(s) was (were) placed outside the HCD tube, at a distance of 0.3 mm, giving rise to a longitudinal discharge.

4.1   *Calculated potential distribution, species densities and sputter flux*

Figure 2 shows the calculated potential distributions (a) and electron density profiles (b) at the cylinder axis ($r = 0$), and the sputter fluxes at the cathode (c) as a function of axial position, for three different conditions in the asymmetric (AC) HCD. The anode ring is positioned at $z = 0$ cm, whereas $z = 5$ cm corresponds to the other open end of the HCD tube. The applied discharge voltage does not vary significantly for the three electrical conditions investigated. It is 375 V at 1 A, 388 V at 2 A and 410 V at 3 A.

It is clear from Fig. 2a that the potential at the cylinder axis varies strongly as a function of axial position, resulting in a considerable axial electric field in the entire discharge tube. The latter gives rise to an electron current in the longitudinal direction, towards the anode, which is responsible for the conduction of the electric current [13]. Moreover, the potential at the cylinder axis, which is in the negative glow (NG) region, appears to be negative in a large part of the

discharge tube. At 1 A, it is only slightly positive (ca. 3 V) near the opening to the anode ring, it becomes zero at about 0.2 cm, and it drops to values of about −110 V at the other end of the HCD ($z = 5$ cm). At higher currents, the potential distribution slightly shifts towards less negative values. At 2 A, the maximum potential is about 11 V, the potential becomes zero at 0.8 cm, and at its most negative value, at the end of the HCD, it is −75 V. At 3 A, the potential drops from almost 20 V at the anode side of the HCD to zero at 1.6 cm, and to −53 V at the other end of the HCD. This negative potential is in contrast to planar cathode-glow discharges, where the potential in the NG, also called the "plasma potential", is typically positive, in order to guarantee the discharge current balance (see, for example, [14]). However, in HCDs there is no need for a positive plasma potential, because the special geometry of the HCD reduces the loss of fast electrons to the anode, and allows a sufficient ion flux towards the cathode.

This phenomenon also explains the potential drop as a function of distance from the anode. Indeed, the electrons emitted from the cathode are more easily lost to the anode at low values of z (i.e. closer to the anode), so that a positive plasma potential is needed here to reduce the electron flux to the anode. At higher values of z (i.e. further away from the anode), the electron loss to the anode is much smaller, so that the potential in the plasma does not need to be positive. Moreover, the influence of the anode, i.e. with potential equal to zero, is not felt at sufficiently long distances from the anode, resulting in a more negative potential in the plasma. A similar potential drop as a function of axial position was also observed by Mizeraczyk, and the plasma potential was also found to be more negative at lower electric currents [7, 8]. Hence, our model calculations give the explanation for the experimental observations.

The calculated electron density profiles at the cylinder axis are plotted in Fig. 2b, for three different electric currents. The electron density reaches its maximum near the anode side, at $z = 0.5$ cm, and it drops by more than about an order of magnitude towards the other end of the discharge tube. The reason for this maximum near the anode side is that the highest (most positive) plasma potential is at this side, giving rise to a strong radial electric field, resulting in high electron en-
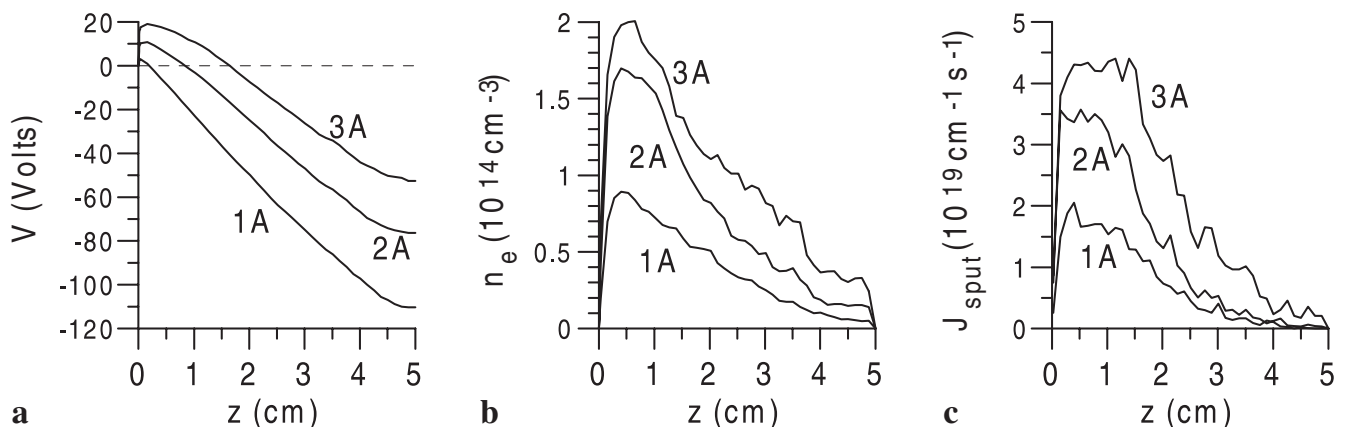

FIGURE 2   Calculated potential (**a**) and electron density (**b**) at the cylinder axis, and the flux of sputtered Cu atoms at the cathode (**c**) as a function of axial position at three different electric currents, in the AC discharge
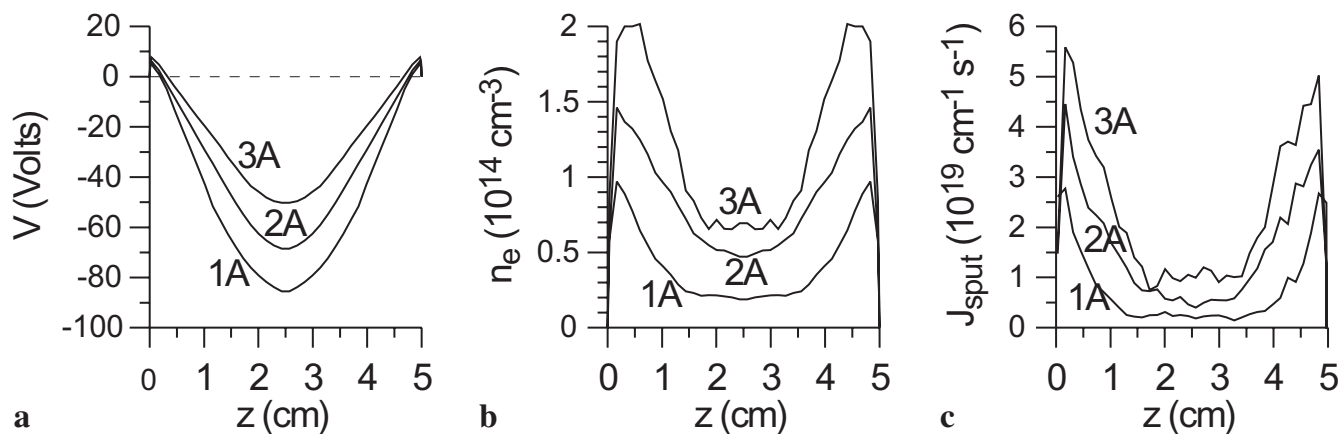
FIGURE 3   Calculated potential (**a**) and electron density (**b**) at the cylinder axis, and the flux of sputtered Cu atoms at the cathode (**c**) as a function of axial position at three different electric currents, in the ACA discharge

ergies and consequently in many electron-impact-ionization collisions, i.e. a high production rate of electrons. Such an asymmetric electron density profile was also reported by Mizeraczyk [8]. The density profiles of the other plasma species were also calculated to be non-uniform in the axial direction, as was demonstrated in [11].

Figure 2c illustrates the calculated fluxes of sputtered Cu atoms at the cylindrical cathode as a function of axial position, at three different electric currents. Again, the flux of sputtered atoms is at its maximum at about 0.5–1 cm from the anode ring, in correlation with the maximum in the electron density profiles. Indeed, as mentioned above, the electron-impact ionization rate is at its maximum here, giving rise not only to the largest production of electrons but also of ions, leading to the highest fluxes of ions (and fast atoms) towards the cathode, and hence the largest amount of sputtering. This theoretical prediction of non-uniform sputter fluxes might have consequences for the lifetime of the laser discharge tube, because the hollow-cathode cylinder might be eroded in a non-uniform way. This phenomenon has also been observed experimentally [15, 16].

Because practical HCD tubes for laser applications are often surrounded by anode rings at both ends (e.g. in a construction of several alternating hollow cathodes and anodes [17–20]), we have also investigated the axial distribution of the above plasma quantities in a symmetric HCD (ACA configuration), and the result is depicted in Fig. 3. The potential at the cylinder axis (Fig. 3a) is again slightly positive at the ends of the HCD tube, near the anode rings, and drops more or less linearly as a function of axial position. Because the HCD is now surrounded by two anode rings, the potential distribution is symmetric, with the most positive values at the ends and the most negative values in the middle of the tube. Again, the plasma potential is found to be most positive near the anode rings and less negative in the middle of the tube at higher electric currents, as shown in Fig. 3a. Both the axial distribution and the effect of electric current are in good correlation with the measurements by Mizeraczyk [7].

The calculated electron density profiles at the cylinder axis (Fig. 3b) and the sputter fluxes at the cathode as a function of axial position (Fig. 3c) reach their maxima at the ends of the tube, near the anode rings, and they show a dip in the middle

of the tube. Hence, it appears that the symmetric HCD tube (ACA) is composed of two asymmetric discharges between one anode ring and half of the HCD tube, and the presence of one asymmetric discharge seems not to affect the other discharge. This was also suggested by Mizeraczyk [7], although it was stated that it does not hold true for very short, symmetric (ACA) HCD tubes.

4.2   *Comparison with experimental data*

In order to verify our calculation results, we have compared them with experimental data for exactly the same cell geometry and discharge conditions. Because most plasma quantities (such as the potential distribution and the plasma species densities) cannot easily be measured, we are limited here to a comparison of the macroscopic quantities, which are more easily accessible, i.e. the electric current and optical emission intensities of He and Cu lines as a function of axial position. The electric current was calculated in our model as the sum of the fluxes of the charged plasma species. The optical emission intensities could not explicitly be calculated in our model, because the level populations of the individual excited levels would have been required. Instead, we calculated the electron-impact excitation rates of He and Cu atoms in the plasma. This is probably a good measure of the optical emission intensities, because electron-impact excitation is expected to be a dominant production mechanism for the excited levels [21].

Figure 4 illustrates the calculated (solid lines) and measured (dashed lines and symbols) linear electric current densities at the cathode, as a function of axial position, for the three different currents investigated, both in the AC discharge (a) and the ACA discharge (b). Both calculated and measured current distributions are characterized by a maximum at the end(s) of the tube, near the anode ring(s), and a minimum at the other end of the HCD tube (AC discharge) or in the middle of the tube (ACA discharge). The agreement between calculated and measured results is reasonable for the AC discharge, although the calculations appear to drop somewhat too rapidly as a function of axial position, especially at the lowest currents. In the ACA discharge, the agreement is less satisfactory; the dip in the calculated current distributions in the middle
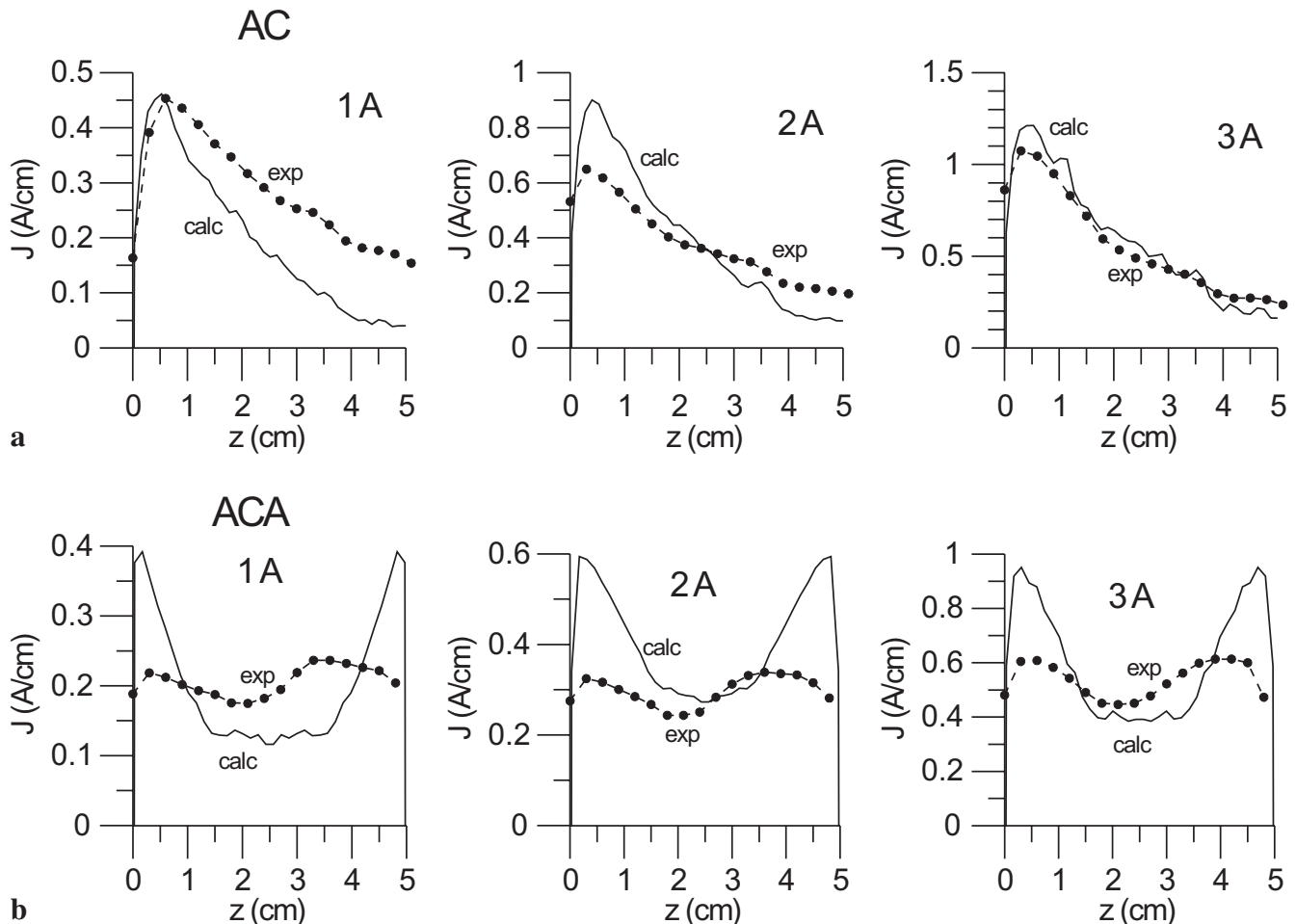
FIGURE 4   Comparison of calculated (*solid lines*) and measured (*dashed lines* and *symbols*) linear electric current densities at the cathode as a function of axial position at three different electric currents, in the AC discharge (**a**) and the ACA discharge (**b**)

of the tube is much more pronounced than in the measured data. Nevertheless, the general behavior of the axial distribution is reasonably well predicted. It shows that the cathode will be primarily bombarded by (energetic) ions at the end(s) of the discharge tube, near the anode ring(s), and that both heating and sputtering of the cathode material will be non-uniformly distributed, probably resulting in a reduced cathode lifetime.

Figure 5 shows the comparison between the calculated electron-impact excitation rates of He atoms, averaged over the radial direction (solid lines, left axis), and the measured optical emission intensities of the He (I) line at 588 nm (dashed lines and symbols; right axis), both in the AC discharge (a) and the ACA discharge (b). Because the measurements at 1 A yielded signal intensities too low, the comparison is only shown for the currents of 2 A and 3 A. In analogy to the current density distributions, the calculated excitation rates and the measured optical emission intensities also exhibit maxima at the end(s) of the HCD tube, near the anode ring(s), and they reach low values, either at the other end of the discharge tube (AC discharge) or in the middle of the tube (ACA discharge). The agreement between the calculated and measured data is fairly good for the AC discharge, but it is again less satisfactory for the ACA discharge, where the calculated excitation rates show a more pronounced dip in the

middle of the tube. Note that both the calculated and measured data are not perfectly symmetric in the ACA discharge. This is attributed to statistical fluctuations in the electron MC model (for the calculated data) and experimental uncertainties in the measured results. Nevertheless, the general trend is again sufficiently predicted.

Finally, the calculated excitation rates of the sputtered Cu atoms, averaged over the radial direction (solid lines, left axis), and the measured optical emission intensities of the Cu (I) 511-nm line (dashed lines and symbols, right axis), are plotted as a function of axial position in Fig. 6, both in the AC discharge (a) and in the ACA discharge (b). Again, the comparison is only made for 2 A and 3 A, because of measured signal intensities being too low at 1 A. In the AC discharge, the calculated position of the maximum is slightly shifted toward the middle of the discharge, in comparison with the measured data. This suggests that the calculated sputtered Cu atom density profile [11] is not yet completely correct. However, in contrast to the above results, the agreement between calculated and measured data is now found to be much better for the ACA discharge. In general, it is clear that although the shapes of the calculation results are not yet in perfect agreement with the experimental data, the overall behavior of the axial distribution of the plasma quantities is correctly predicted.
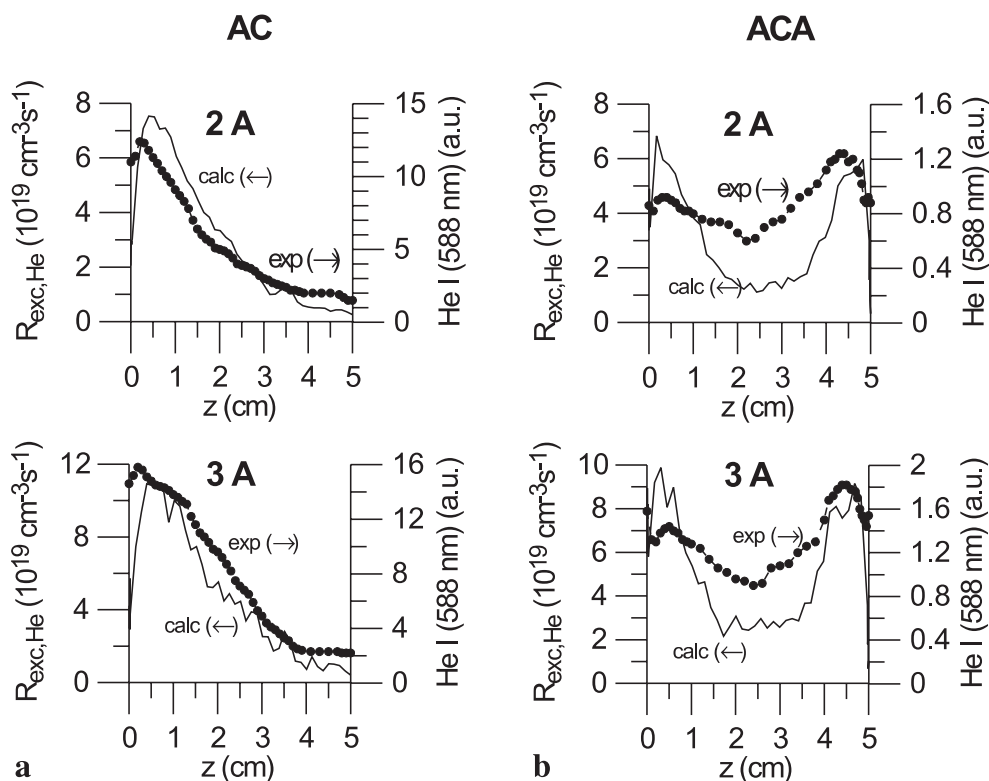
FIGURE 5 Comparison of calculated excitation rates of He atoms, averaged over the radial direction (*solid lines*; *left axis*) and measured He (I) 588 nm optical emission intensities (*dashed lines* and *symbols*; *right axis*) as a function of axial position at two different electric currents, in the AC discharge (**a**) and the ACA discharge (**b**)
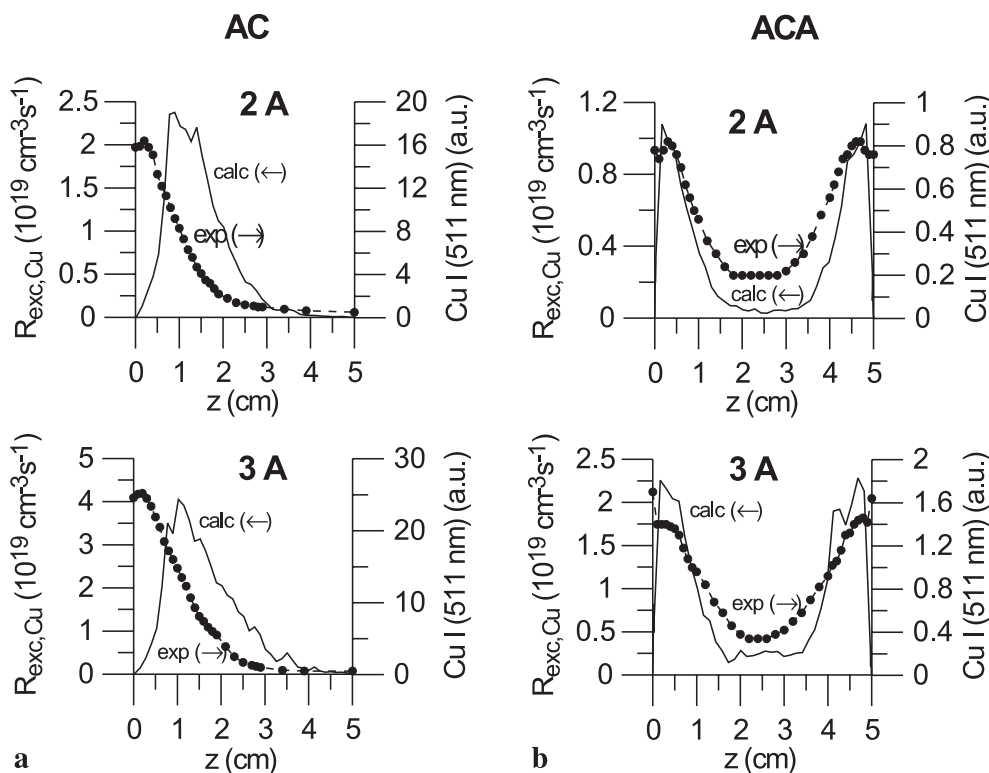

FIGURE 6 Comparison of calculated excitation rates of Cu atoms, averaged over the radial direction (*solid lines*; *left axis*) and measured Cu (I) 511 nm optical emission intensities (*dashed lines* and *symbols*; *right axis*) as a function of axial position at two different electric currents, in the AC discharge (**a**) and the ACA discharge (**b**)

5   Conclusion

The axial non-uniformity of longitudinal HCD tubes has been investigated by means of a numerical model, developed for a copper HCD in a mixture of helium and argon. Two kinds of longitudinal HCD tubes have been studied: an asymmetric discharge with an anode ring at one end of the HCD tube (AC discharge), and a symmetric discharge, with two anode rings at both ends of the cathode tube (ACA discharge).

In the AC discharge, the calculated plasma potential (at the cylinder axis) dropped considerably as a function of axial position, from a slightly positive value (ca. 3–20 V) near the anode ring to clearly negative values (ca. -53 to -110 V, depending on the discharge conditions) at the other end of the discharge tube. This resulted in a rather strong axial electric field through the HCD tube (with values typically in the order of 20 V/cm), and hence in a considerable electron current toward the anode. Moreover, because the radial electric field was strongest near the anode ring (i.e. where the plasma potential was most positive), the electrons had higher energies and gave rise to more ionization collisions at the beginning of the discharge tube, near the anode ring. This resulted in a non-uniform electron density profile, with a peak near the opening to the anode ring. Also, most other calculated plasma quantities, such as the densities of other species, the flux of sputtered Cu atoms from the cathode, the current density at the cathode and the electron-impact ionization and excitation rates, were characterized by a non-uniform distribution, with a peak near the open end of the discharge tube, adjacent to the anode ring.

As a practical laser set-up often consists of alternating hollow cathodes and anodes, the same plasma quantities were also calculated for the ACA discharge, where the hollow cathode was surrounded by two anode rings at both ends. The calculated plasma quantities in the ACA discharge appeared to be fairly symmetric, with a maximum at the ends of the tube, near the two anode rings, and a dip in the middle of the discharge tube. Hence, it is suggested that the ACA discharge is composed of two more or less independent, asymmetric AC discharges, with lengths equal to half of the ACA discharge tube.

It is worth mentioning that the shape of this longitudinal HCD (i.e. with 5-cm length and 4-mm inner diameter) would suggest that a 1D model (in the radial direction) is sufficient to describe its characteristics. However, the calculated axial non-uniformity clearly demonstrates that in fact a 2D model is necessary for a realistic representation.

To verify our calculations, the calculated current density and excitation rates of He and Cu atoms as a function of axial position were compared with current densities and optical emission intensities, measured for exactly the same discharge conditions and tube geometry. Although the calculated and measured axial distributions did not perfectly coincide, the agreement was considered to be satisfactory because the predicted peaks and dips in the calculation results were also found in the measured data.

In conclusion, it is suggested that the axial non-uniformity of the HCD will affect the operation of the laser tube. Indeed, because the cathode will be primarily bombarded by (energetic) ions at the ends of the discharge tube, near the anode ring(s), both heating and sputtering of the cathode material will be non-uniformly distributed, probably resulting in a reduced lifetime of the cathode. Moreover, because the plasma is most intense near the ends of the tube, adjacent to the anode ring(s), it is expected that some part of the HCD will be inactive, reducing the active length of the laser tube. Hence, this explains why increasing the length of the discharge tube does not always give rise to more intense lasers [17]. It is therefore more interesting to use a set-up composed of several alternating short, hollow cathodes and anodes [17–20].

REFERENCES

1 D.C. Gerstenberger, R. Solanki, G.J. Collins: IEEE J. Quantum Electron. **QE-16**, 820 (1980)
2 I.G. Ivanov, E.L. Latush, M.F. Sem: *Metal Vapor Ion Lasers: Kinetic Processes and Gas Discharges* (Wiley, Chichester 1996)
3 P.J. Slevin, W.W. Harrison: Appl. Spectrosc. Rev. **10**, 201 (1975)
4 S. Caroli: Prog. Anal. Atom. Spectrosc. **6**, 253 (1983)
5 A. Goldamn, J. Amoroux: *Gases: Macroscopic Processes and Discharges* (Plenum Press, New York 1983)
6 K. Rozsa: Z. Naturforsch. A **35**, 649 (1980)
7 J. Mizeraczyk: Acta Phys. Hung. **54**, 71 (1983)
8 J. Mizeraczyk: J. Phys. D: Appl. Phys. **20**, 429 (1987)
9 J. Mizeraczyk, J. Wasilewski, J. Konieczka, W. Urbanik, M. Grozeva, J. Pavlik: Proc. Int. Conf. Lasers '81, ed. by V.A. Mc Lean (STS Press, New Orleans 1981) pp. 877–881
10 J. Mizeraczyk, M. Neiger, J. Steffen: IEEE J. Quantum Electron. **QE-20**, 1233 (1984)
11 A. Bogaerts, R. Gijbels: J. Appl. Phys., in press: December 1, 2002
12 A. Bogaerts, R. Gijbels, V.V. Serikov: J. Appl. Phys. **87**, 8334 (2000)
13 R.R. Arslanbekov, A.A. Kudryavtsev, R.C. Tobin: Plasma Sources Sci. Technol. **7**, 310 (1998)
14 A. Bogaerts, R. Gijbels, W.J. Goedheer: J. Appl. Phys. **78**, 2233 (1995)
15 J. Hamisch, J. de la Rosa: Appl. Phys. B **43**, 189 (1987)
16 J. Yu, R. Macdonald: J. Phys. D: Appl. Phys. **22**, 1627 (1989)
17 H.J. Eichler, H.J. Koch, J. Salk, G. Schäfer: IEEE J. Quantum Electron. **QE-15**, 908 (1979)
18 B.E. Warner, D.C. Gerstenberger, R.D. Reid, J.R. McNeil, R. Solanki, K.B. Persson, G.J. Collins: IEEE J. Quantum Electron. **QE-14**, 568 (1978)
19 H.J. Eichler, H. Koch, J. Salk, C. Skrobol: Opt. Commun. **34**, 228 (1980)
20 H.J. Eichler, J. Hamisch, S. Song: Opt. Commun. **61**, 61 (1987)
21 L.L. Alves, G. Gousset, C.M. Ferreira: J. Phys. D: Appl. Phys. **25**, 1713 (1992)